# Normal State of $Nd_{1-x}Sr_xNiO_2$ from Self-Consistent $GW + EDMFT$

Francesco Petocchi,[1] Viktor Christiansson,[1] Fredrik Nilsson,[2] Ferdi Aryasetiawan,[2] and Philipp Werner[1]
[1]Department of Physics, University of Fribourg, 1700 Fribourg, Switzerland
[2]Department of Physics, Division of Mathematical Physics, Lund University, Professorsgatan 1, 223 63 Lund, Sweden

(Received 15 June 2020; revised 3 September 2020; accepted 12 October 2020; published 8 December 2020)

Superconductivity with a remarkably high $T_c$ has recently been observed in hole-doped $NdNiO_2$, a material that shares similarities with the high-$T_c$ cuprates. This discovery promises new insights into the mechanism of unconventional superconductivity, but at the modeling level, there are fundamental issues that need to be resolved. While it is generally agreed that the low-energy properties of cuprates can, to a large extent, be captured by a single-band model, there has been a controversy in the recent literature about the importance of a multiband description of the nickelates. Here, we use a multisite extension of the recently developed $GW + EDMFT$ method, which is free of adjustable parameters, to self-consistently compute the interaction parameters and electronic structure of hole-doped $NdNiO_2$. This full *ab initio* simulation demonstrates the importance of a multiorbital description, even for the undoped compound, and it produces results for the resistivity and Hall conductance in qualitative agreement with experiment.

DOI: 10.1103/PhysRevX.10.041047

Subject Areas: Computational Physics, Condensed Matter Physics, Strongly Correlated Materials

## I. INTRODUCTION

The recent discovery of superconductivity in hole-doped $NdNiO_2$ thin films [1–3] has captivated the condensed matter physics community. Such compounds with a formal $Ni^+$ valence have been theoretically proposed as possible analogues of the cuprates [4,5], and the exploration of their electronic structure and pairing mechanism may provide important insights into the phenomenon of unconventional superconductivity. $NdNiO_2$ is isostructural with $CaCuO_2$, which exhibits high-temperature superconductivity upon hole doping. Ni is coordinated with two oxygens, forming $NiO_2$ square planes, separated by Nd as a spacer cation [4–6]. It has the uncommon oxidation value of $+1$, resulting in a $d^9$ electronic configuration. Despite these obvious similarities with the cuprate superconductors [7], there are also relevant differences between the nickelates and cuprates. The energy splitting between the Ni $3d$ levels and the O $2p$ levels is almost twice as large as the corresponding splitting in $CaCuO_2$ [5,8,9], which puts $NdNiO_2$ into the Hubbard regime rather than the charge transfer regime [10], and possibly precludes the formation of Zhang-Rice singlets. The peculiar structure with missing apical oxygens significantly alters the crystal field: Several density functional theory (DFT) [11] calculations [6,9,12,13] have shown that the $3d_{z^2}$ orbital is lower than the $3d_{x^2-y^2}$ orbital, and they predicted the presence of additional Fermi pockets at the Γ and A points. There is a single nickel-centered band of $3d_{x^2-y^2}$ character crossing the Fermi level, and this band has a significant hole concentration due to self-doping from Nd-$5d$ states, which indicates an important role played by the low-lying Nd $5d_{z^2}$ and $5d_{xy}$ bands.

While the DFT band structure is well established, there is a general consensus about the strongly correlated nature of the material, which requires a full many-body description of a physically motivated low-energy model. On the other hand, there is an intense debate about the number of Ni bands that need to be included in a realistic low-energy model. Some authors have argued that the nickelates are an almost perfect realization of a single-orbital Hubbard model [6,14], while other groups have emphasized the modest splittings between the Ni $3d$ bands, relative to the Hund coupling, the importance of high-spin configurations, and other multiorbital aspects [5,8,13,15]. The origin of this controversy is that studies based entirely on DFT calculations miss important correlation and multiorbital effects induced by Hund coupling, while model calculations or simulations based on the combination of DFT and dynamical mean field theory (DMFT) [16] involve *ad hoc* parameters and double-counting corrections that substantially affect the results.

*Published by the American Physical Society under the terms of the Creative Commons Attribution 4.0 International license. Further distribution of this work must maintain attribution to the author(s) and the published article's title, journal citation, and DOI.*

In addition, on the experimental side, the new nickelate superconductor defies naive expectations: Contrary to the cuprates, the undoped parent compound is weakly metallic, and no evidence of an antiferromagnetically ordered state has been found so far [1,2]. This observation challenges the widespread assumption of a key role played by antiferromagnetic spin fluctuations in the unconventional pairing mechanism. The superconducting dome is similar to that of hole-doped $La_2CuO_4$ but with a narrower doping window, a smaller $T_c \sim 10$ K, and a double-peak structure [2,3]. Both on the underdoped and overdoped sides, superconductivity emerges from a bad metallic (weakly insulating) state. A recent spectroscopic study [17] supports the multiorbital Mott-Hubbard picture but also finds weak indications for the formation of Zhang-Rice singlets [18].

Here, we employ the recently developed multitier $GW$ + EDMFT method [19–21], which enables an *ab initio* simulation of strongly correlated materials *without* adjustable parameters, apart from the choice of the low-energy space, to clarify the electronic structure and the importance of multiorbital physics in undoped and hole-doped $NdNiO_2$. For this purpose, we extend the $GW$ + EDMFT method to two coupled, interacting, low-energy models for nickel and neodymium containing five and two bands, respectively. This low-energy theory with self-consistently computed, dynamically screened, interaction parameters is embedded without double counting of interaction energies into an *ab initio* band structure, as illustrated in Fig. 1. Our computational scheme starts with a DFT calculation in the local density approximation (LDA) [22], where we employ the virtual crystal approximation (VCA) [23] to realistically account for the shifts of the bands induced by hole doping. The downfolding to the low-energy subspace hosting the Nd and Ni bands is achieved with a single-shot $G^0W^0$ calculation. In this way, the high-energy degrees of freedom are incorporated via a frequency- and momentum-dependent self-energy and polarization into the bare propagators and bare interactions of the low-energy model. The latter is solved using self-consistent $GW$ + EDMFT, with separate extended DMFT (EDMFT) [24] impurity models for Nd and Ni. The $GW$ + EDMFT formalism [25] captures different aspects of interacting electron systems: $GW$ [26] describes collective long-range charge fluctuations and dynamical screening effects, while EDMFT, the extension of DMFT to systems with nonlocal interactions [24], captures the effect of local Coulomb repulsions. These two techniques are combined by replacing the local part of the $GW$ self-energy and polarization with the corresponding EDMFT estimates. Both the fermionic and bosonic dynamical mean fields, represented, respectively, by the hybridization function and interaction tensor, are updated in the self-consistency loop, resulting in a parameter-free *ab initio* simulation, which only requires the definition of a physically motivated low-energy space. All calculations were performed at a temperature of $T = 0.1$ eV.

## II. METHODS

Our simulations are based on the parameter-free multitier $GW$ + DMFT scheme [19–21], which treats different energy scales with appropriate levels of accuracy and which self-consistently computes dynamically screened interactions for the low-energy model space.

The initial LDA calculations are performed using the full-potential, linearized, augmented, plane-wave code FLEUR [27], with the experimental lattice parameters for $NdNiO_2$ ($a = b = 3.92$ Å, $c = 3.28$ Å [28]), and a $16 \times 16 \times 16$ $k$-point grid. The crystal symmetry belongs to the $P4/mmm$ space group. The nickel Wyckoff position is

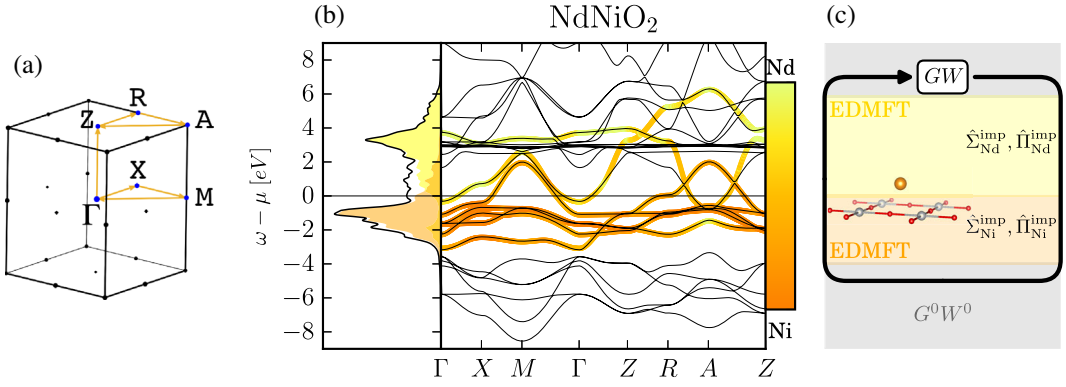


FIG. 1. Low-energy model and computational scheme. (a) First Brillouin zone of $NdNiO_2$ and high-symmetry lines. (b) LDA band structure and low-energy space spanned by seven bands of predominantly Nd and Ni character. (c) Schematic representation of the multitier $GW$ + EDMFT framework: In a first step, the bare propagators and frequency-dependent bare interactions of the low-energy model are obtained from a single-shot $G^0W^0$ downfolding. Then, two impurity problems, for Ni and Nd, respectively, are defined and self-consistently solved considering retarded interactions, which account for screening effects. To the corresponding local self-energies and polarizations, we add nonlocal contributions evaluated at the $GW$ level. These frequency- and momentum-dependent objects enter into the EDMFT lattice self-consistency loop.

(0,0,0)-(1a), the one of neodymium is (0.5,0.5,0.5)-(1d), and for oxygen it is (0.5,0,0)-(2f). To treat the $4f$ states, which appear unphysically close to the Fermi energy, we use a manual core setup with the $4f^3$ electrons in the core. To also correct the bands originating from the unoccupied $4f$ states, we use a self-consistent LDA + $U$ + cRPA (constrained random phase approximation) approach, where the cRPA $U$ [29] calculated for the unoccupied $4f$ bands is used in a new LDA + $U$ calculation iteratively until convergence is reached. To simulate the doped compound, we use the VCA, where the doping is achieved by replacing a fraction of Nd with Pr, instead of the experimentally used Sr. This procedure is due to a technical limitation, which only allows us to dope with consecutive elements; see Supplemental Material (SM) [30]. The low-energy model is defined using maximally localized Wannier functions obtained from the Wannier90 library [31–34], while the $G^0W^0$ calculations are performed using the SPEX code [35], with $8\times8\times8$ $k$ points and 250 bands.

Within the low-energy space with two Nd and five Ni orbitals, we perform a self-consistent $GW$ + EDMFT calculation. In this approach, local self-energies $\hat{\Sigma}^{\mathrm{imp}}$ and polarizations $\hat{\Pi}^{\mathrm{imp}}$ for Nd and Ni are computed from separate EDMFT impurity problems with self-consistently optimized fermionic and bosonic Weiss fields $\mathcal{G}$ and $\mathcal{U}$, respectively. To these local impurity self-energies and polarizations, we add the nonlocal $GW$ components,

$$\Sigma^{\mathrm{nonloc}}_{ab}(\mathbf{q},\tau) = -\sum_{\mathbf{k}cd} G_{cd}(\mathbf{k},\tau) W_{acbd}(\mathbf{q}-\mathbf{k},\tau) + \sum_{cd} G^{\mathrm{loc}}_{cd}(\tau) W^{\mathrm{loc}}_{acbd}(\tau), \tag{1}$$

$$\Pi^{\mathrm{nonloc}}_{acbd}(\mathbf{q},\tau) = \sum_{\mathbf{k}} G_{ab}(\mathbf{k},\tau) G_{dc}(\mathbf{k}-\mathbf{q},-\tau) - G^{\mathrm{loc}}_{ab}(\tau) G^{\mathrm{loc}}_{dc}(-\tau), \tag{2}$$

where $W_{acbd}$ denotes the elements of the screened interaction and $G_{ab}$ those of the interacting Green's function. The $GW$ + EDMFT cycle starts from an initial guess for $\hat{\Sigma}^{\mathrm{imp}}$ and $\hat{\Pi}^{\mathrm{imp}}$. Then, given the noninteracting lattice Hamiltonian $\hat{\mathcal{H}}(\mathbf{k})$ for the localized Wannier orbitals of the low-energy space, nonlocal $GW$ self-energies and polarizations are computed. The sum of these two contributions yields the momentum-dependent self-energy $\Sigma_{\mathbf{k}}$ and polarization $\Pi_{\mathbf{q}}$ entering the lattice sums,

$$\hat{G}^{\mathrm{loc}} = \frac{1}{N}\sum_{\mathbf{k}} ((\hat{G}^{(0)}_{\mathbf{k}})^{-1} - \hat{\Sigma}_{\mathbf{k}})^{-1}, \tag{3}$$

$$\hat{W}^{\mathrm{loc}} = \frac{1}{N}\sum_{\mathbf{q}} \hat{U}_{\mathbf{q}} (\mathbb{1} - \hat{\Pi}_{\mathbf{q}}\hat{U}_{\mathbf{q}})^{-1}, \tag{4}$$

where $\hat{G}^{(0)}_{\mathbf{k}}$ is the noninteracting propagator of the low-energy subspace, which also incorporates the $G^0W^0$ contribution [see Eq. (9) below], and $\hat{U}_{\mathbf{q}}$ the "bare" Coulomb interaction resulting from the initial $G^0W^0$ downfolding. These local Green's functions and screened interactions are obtained by inversion in the full $(7\times7)$ orbital space. The EDMFT self-consistency condition then demands that the projections of $\hat{G}^{\mathrm{loc}}$ and $\hat{W}^{\mathrm{loc}}$ onto the Ni and Nd sites are equal to the impurity Green's functions and screened interactions for these sites. Using these $G^{\mathrm{imp}}$ and $W^{\mathrm{imp}}$ and the impurity self-energies and polarizations, the fermionic and bosonic Weiss fields are computed as

$$\hat{\mathcal{G}}_i = (\hat{\Sigma}^{\mathrm{imp}}_i + (\hat{G}^{\mathrm{imp}}_i)^{-1})^{-1} \quad i\in\{\mathrm{Ni},\mathrm{Nd}\}, \tag{5}$$

$$\hat{\mathcal{U}}_i = \hat{W}^{\mathrm{imp}}_i (\mathbb{1} + \hat{\Pi}^{\mathrm{imp}}_i \hat{W}^{\mathrm{imp}}_i)^{-1} \quad i\in\{\mathrm{Ni},\mathrm{Nd}\}, \tag{6}$$

and used as inputs for the two EDMFT impurity problems. (In these inversions, all orbital indices are restricted to either the Ni or Nd sites.) An efficient continuous-time Monte Carlo solver [36,37] for models with dynamically screened interactions [38] then yields the impurity Green's functions $\hat{G}^{\mathrm{imp}}_i$ and density-density correlation functions $\hat{\chi}^{\mathrm{imp}}_i$. After the Fourier transformation of $\hat{G}^{\mathrm{imp}}_i$ and $\hat{\chi}^{\mathrm{imp}}_i$, the new $\hat{\Sigma}^{\mathrm{imp}}_i$ and $\hat{\Pi}^{\mathrm{imp}}_i$ are computed from the Weiss fields, the impurity Green's functions, and charge susceptibilities:

$$\hat{\Sigma}^{\mathrm{imp}}_i = \hat{\mathcal{G}}^{-1}_i - (\hat{G}^{\mathrm{imp}}_i)^{-1} \quad i\in\{\mathrm{Ni},\mathrm{Nd}\}, \tag{7}$$

$$\hat{\Pi}^{\mathrm{imp}}_i = \hat{\chi}^{\mathrm{imp}}_i (\hat{\mathcal{U}}_i \hat{\chi}^{\mathrm{imp}}_i - \mathbb{1})^{-1} \quad i\in\{\mathrm{Ni},\mathrm{Nd}\}. \tag{8}$$

Since all the self-energy and polarization contributions in this multitier scheme are diagrammatically defined, we can connect the different subspaces in a consistent way, without any double counting. The explicit expressions for the interacting lattice Green's functions and screened interactions are

$$G^{-1}_{\mathbf{k}} = \overbrace{i\omega_n + \mu - \varepsilon^{\mathrm{DFT}}_{\mathbf{k}} + V_{\mathrm{XC},\mathbf{k}} - (\Sigma^{G^0W^0}_{\mathbf{k}} - \Sigma^{G^0W^0}_{\mathbf{k}}|_I)}^{\mathrm{LDA}+G^0W^0,G^{0\,-1}_{I,\mathbf{k}}} \underbrace{-(\Sigma^{GW}_{\mathbf{k}}|_I - \Sigma^{GW}|_{C,\mathrm{loc}} + \Delta V_H|_I)}_{GW} \underbrace{-\Sigma^{\mathrm{EDMFT}}|_{C,\mathrm{loc}}}_{\mathrm{EDMFT}}, \tag{9}$$

$$W^{-1}_{\mathbf{q}} = \overbrace{v^{-1}_{\mathbf{q}} - (\Pi^{G^0G^0}_{\mathbf{q}} - \Pi^{G^0G^0}_{\mathbf{q}}|_I)}^{\mathrm{cRPA}+G^0W^0,U^{-1}_{I,\mathbf{q}}} \underbrace{-(\Pi^{GG}_{\mathbf{q}}|_I - \Pi^{GG}|_{C,\mathrm{loc}})}_{GW} \underbrace{-\Pi^{\mathrm{EDMFT}}|_{C,\mathrm{loc}}}_{\mathrm{EDMFT}}, \tag{10}$$

where $C$ refers to the strongly correlated local subspaces (treated with EDMFT) and $I$ to the full seven-orbital subspace in which the $GW$ calculation is performed. Note that $\Delta V_H$ is the Hartree contribution to the self-energy, $v_{\mathbf{q}}$ is the bare interaction and $V_{\mathrm{XC}}$ the exchange-correlation potential (which is replaced by the $G^0W^0$ self-energy). A detailed derivation of the multitier $GW+\mathrm{EDMFT}$ approach can be found in Refs. [20,21].

## III. RESULTS

### A. Occupation and spin statistics

A useful feature of this EDMFT-based method is that it gives access to the relevant occupation and spin states on Ni and Nd. In Fig. 2(a), we present the corresponding histograms for different hole dopings. Even in the undoped compound, where the total density is fixed at the LDA nominal value, the configuration probabilities $P^{(n)}$, which measure the fraction of time spent in the indicated atomic configurations, clearly reveal the multiorbital behavior of the nickel subsystem: The $3d^8$ states are relevant and comparable in magnitude to the naively expected $3d^9$ states; also, the charge fluctuations to the $3d^7$ states cannot be ignored. This distribution is largely due to the self-doping from Nd, which accommodates up to two electrons. Interestingly, the configuration probabilities of Ni vary with the dopant concentration in a nonmonotonic fashion. In agreement with the results from LDA + $U$ studies [39], we find that the doped holes essentially end up on the Nd sites, as can be concluded from the monotonous increase in the $5d^0$ configuration. The nonmonotonic behavior observed on the Ni sites, which have an electron density pinned at 8.3 (see also SM [30]), results from doping-induced changes in the hybridization strength and the self-consistently computed interaction parameters. In the following matrices, we report, for the undoped and the optimally doped compounds, the screened values of the effective Ni on-site interaction $\mathcal{U}(\omega_n=0)$ in the upper triangular section and the effective Hund coupling $\mathcal{J}(\omega_n=0)$ in the lower one:

$$\hat{\mathcal{I}}^{\delta=0.0}_{\mathrm{Ni}} = \begin{array}{c|ccccc} & d_{xz} & d_{yz} & d_{xy} & d_{z^2} & d_{x^2-y^2} \\ \hline d_{xz} & 4.95 & 3.50 & 3.39 & 3.82 & 3.08 \\ d_{yz} & 0.69 & 4.95 & 3.39 & 3.82 & 3.08 \\ d_{xy} & 0.69 & 0.69 & 4.74 & 3.07 & 3.54 \\ d_{z^2} & 0.50 & 0.50 & 0.71 & 4.85 & 2.82 \\ d_{x^2-y^2} & 0.53 & 0.53 & 0.35 & 0.57 & 3.98 \end{array}, \quad (11)$$

$$\hat{\mathcal{I}}^{\delta=0.2}_{\mathrm{Ni}} = \begin{array}{c|ccccc} & d_{xz} & d_{yz} & d_{xy} & d_{z^2} & d_{x^2-y^2} \\ \hline d_{xz} & 5.24 & 3.81 & 3.62 & 4.18 & 3.29 \\ d_{yz} & 0.68 & 5.24 & 3.62 & 4.18 & 3.29 \\ d_{xy} & 0.67 & 0.67 & 4.85 & 3.35 & 3.66 \\ d_{z^2} & 0.49 & 0.49 & 0.70 & 5.32 & 3.09 \\ d_{x^2-y^2} & 0.51 & 0.51 & 0.34 & 0.56 & 4.07 \end{array}. \quad (12)$$

In particular, we notice that the $\mathcal{J}$ values decrease with hole doping [see also Fig. 2(c)], while the interorbital interactions increase more strongly than the intraorbital ones.

In a strongly correlated, half-filled single-band model, one would expect to find spins with magnitude $|S_z|$ close to one-half and fluctuations to states with $|S_z|=0$. As can be seen from Fig. 2(b), in our seven-orbital model, fluctuations to both high- and low-spin states are significant. The high-spin states are stabilized by the Hund coupling. Even if the doping-dependent changes on the Ni ion are small, the nonmonotonicity in the charge and spin statistics indicates that the optimally doped compound is closest to the behavior one would expect from a model containing a single $d_{x^2-y^2}$ band and that the expected increase in the population of spin-1 moments with hole doping [5,8,15] only sets in on the overdoped side of the experimental $T_c$ dome.

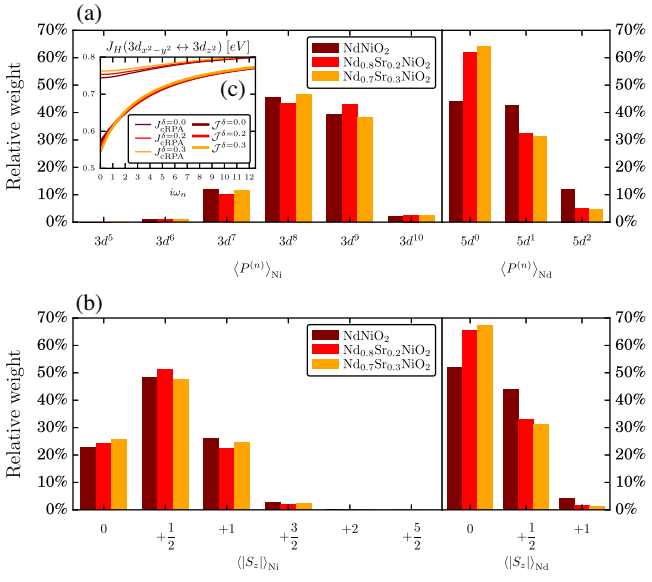


FIG. 2. Occupation and spin statistics for Ni and Nd. (a) Probability distributions for the Ni (left) and Nd (right) atoms to be in the indicated charge states. (b) Probability distributions for the absolute value of the $z$ component of the spin. The different colors correspond to different hole dopings (dark red, undoped; red, close to optimal doping; orange, overdoped). (c) Frequency and doping dependence for the Hund coupling between Ni-$3d_{x^2-y^2}$ and Ni-$3d_{z^2}$.

### B. Local energy renormalizations

The multiorbital nature of the undoped and hole-doped nickelate compounds is the consequence of local energy renormalizations induced by the local EDMFT self-energies. In particular, we find a strong frequency dependence of the real part of $\hat{\Sigma}^{\mathrm{Ni}}_{\mathrm{loc}}$, which is positive and (except

for the $d_{x^2-y^2}$ orbital) increasing with decreasing energy. As a consequence, local energies that correspond to fully occupied orbitals at high energy become available for low-energy holelike charge fluctuations (or fast virtual charge excitations), in agreement with the previously discussed configurational statistics. To demonstrate this effect of the self-energy, we present in Fig. 3 the local energies obtained using three different approaches. We first consider the diagonal entries of the real-space LDA Hamiltonian at the origin, $\epsilon^{\mathrm{LDA}} = \mathcal{H}^{\mathrm{LDA}}(\mathbf{R}=0) - \mu$. In agreement with the LDA results reported in the literature [6,12], this method yields a picture compatible with a single-band description. To represent the local energies of the interacting system, we consider the center of mass of the local spectral function, $\epsilon_\infty = \int \omega A(\omega) d\omega$. (This center of mass includes all the self-energy terms connecting the different tiers, while just adding the real part of the local EDMFT self-energy to $\epsilon^{\mathrm{LDA}}$ would, for example, miss the *GW* contributions.) Also in this picture, which may be thought of as the Hartree limit of our result, the Ni states are mostly occupied, except for the $3d_{x^2-y^2}$ orbital. Finally, to illustrate the effect of the frequency dependence of $\mathrm{Re}\hat{\Sigma}^{\mathrm{Ni}}_{\mathrm{loc}}(\omega_n)$, we recall that the fermionic Weiss field $\hat{\mathcal{G}}^{-1} = i\omega_n + \mu - E_{\mathrm{loc}} - \hat{\Delta}(\omega_n)$ [with $\hat{\Delta}(\omega_n)$ the hybridization function] is defined with respect to an effective local energy $E_{\mathrm{loc}}$ determined by the self-consistency equations. In particular, $E_{\mathrm{loc}}$ incorporates the modifications of the band structure in the downfolding and the $\mathbf{k}$-dependent *GW* contributions to the self-energy. In the EDMFT impurity calculation, the local self-energy is then added by the solver to this effective level. Thus, we plot, in the right-hand level diagrams, the renormalized impurity level positions $\epsilon_0 = E_{\mathrm{loc}} - \mu + \mathrm{Re}\Sigma(0)$. The result indicates a substantial shift of the $3d_{z^2}$ and $3d_{xz,yz}$ orbitals to higher energies, compared to the Hartree limit, while the $3d_{x^2-y^2}$ and $3d_{xy}$ orbitals shift to lower energies. The arrows in the level diagrams demonstrate that increasing the frequency $\omega_n$, where the self-energy is evaluated, to 3 eV (approximate bandwidth) brings the levels closer to their $\epsilon_\infty$ values. In recent LDA + DMFT studies, Lechermann [9,13] emphasized the behavior of the Ni-$3d_{z^2}$ orbital, which, for a large value of the on-site interaction ($U = 10$ eV),

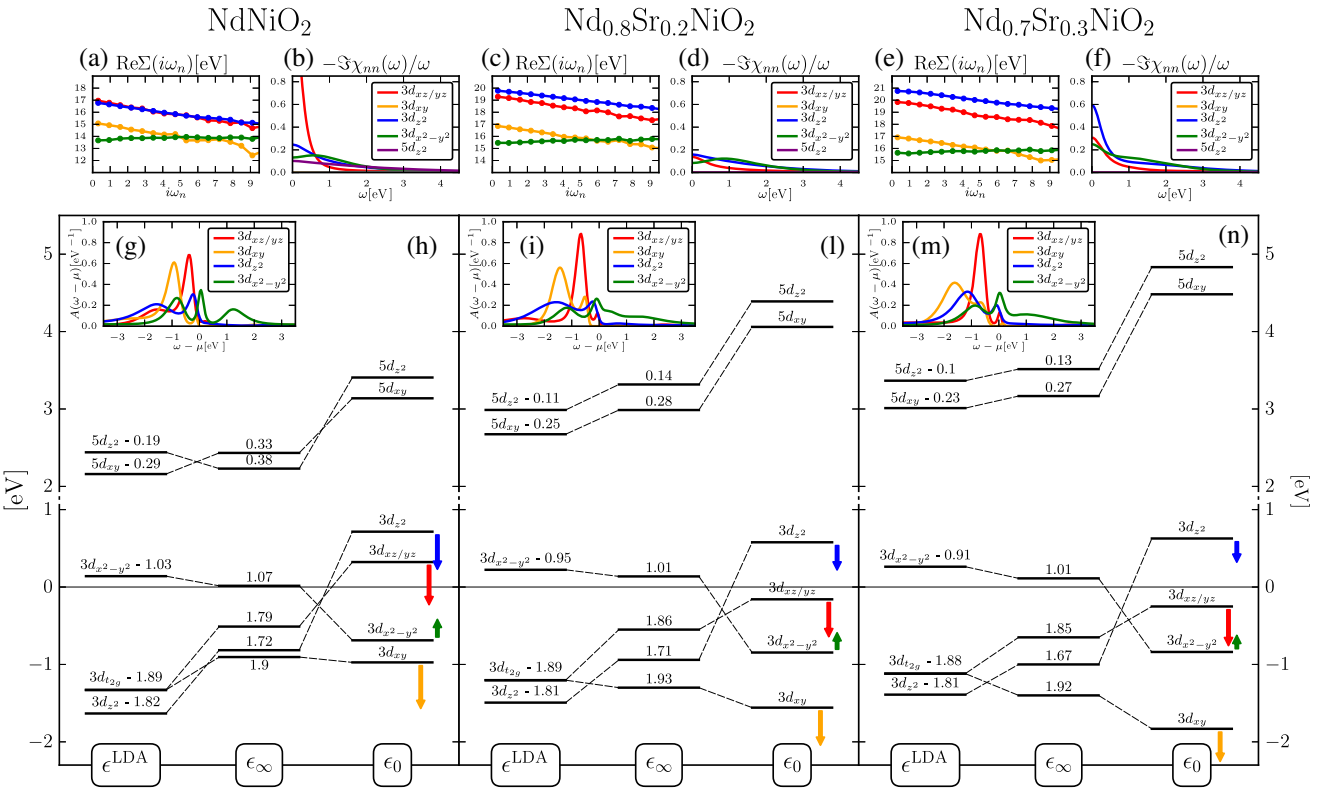


FIG. 3. Level diagrams and energy-dependent shifts of the accessible states. The results for the indicated dopings are summarized in the main panels (h), (l), and (n). The level diagrams on the left, marked with $\epsilon^{\mathrm{LDA}}$, show the average energies of the LDA bands. The level diagrams in the middle, marked $\epsilon_\infty$, indicate the center of mass of the correlated density of states, which is plotted in panels (g), (i), and (m). The level diagrams on the right, marked $\epsilon_0$, indicate the level energies of the EDMFT impurity problems, shifted by $\mathrm{Re}\Sigma(\omega_n = 0)$. Energies are plotted relative to the chemical potential, and the numbers near the levels report the orbital occupations. To illustrate the effect of the $\omega_n$ dependence of the self-energy, shown in panels (a), (c), and (e), we illustrate with arrows the level shift produced by increasing $\omega_n$ to 3 eV (except for the green arrow, where we used 10 eV for a better visualization of the shift direction). Panels (b), (d), and (f) show the charge susceptibilities for different orbitals on the real-frequency axis.

empties out and thus enables the system to undergo an orbital selective Mott transition. Similar multiorbital behavior has also been reported in Refs. [40,41]. Even though our self-consistently computed, static, on-site interactions are a factor of 2 smaller, the result in Fig. 3 is reminiscent of this phenomenology. The same tendency can be seen in the Ni-$3d_{z^2}$ dispersion of the interacting system (see SM Figs. 6–8 [30]) in which the flat part of the band is shifted up in energy very close to the Fermi level.

As a further support of our interpretation, we plot in Figs. 3(b), 3(d), and 3(f) the Fourier transforms of the local charge susceptibilities $\hat{\chi}_{nn}(\tau) = \langle \hat{n}(\tau)\hat{n}(0)\rangle$ on the real frequency axis. This quantity defines the screening due to local charge fluctuations, and the contribution of each orbital is easily identifiable. As expected, no contribution is found from Ni-$3d_{xy}$ and Nd-$5d_{xy}$, which are, respectively, completely filled and completely empty, while Nd-$5d_{z^2}$ contributes only in undoped $NdNiO_2$, which hosts the hole pocket at the Γ point. Ni-$3d_{xz/yz}$ fluctuates strongly in the undoped compound, in agreement with the energy-dependent shift of the effective level position (red arrow). Overall, the optimally doped compound is least affected by charge fluctuations, which suggests that the latter do not play a role in the pairing mechanism.

### C. Fermi surface reconstruction

In Fig. 4, we show how the tight-binding Fermi surfaces are modified by the interactions. The interacting result corresponds to the trace of the **k**-resolved spectral function evaluated at $\omega = 0$. In agreement with the existing literature [6,9,12,39], our noninteracting reference system contains two hole pockets centered at the A and Γ points, associated with Nd-$5d_{xy}$ and Nd-$5d_{z^2}$ states, respectively. LDA predicts that this latter band is continuously pushed above the Fermi level as the hole doping is increased. On top of this shift, our results, already at the $G^0W^0$ level, indicate a substantial flattening of the bands along the Γ-X and Γ-M directions [see SM [30] and sketch of the Brillouin zone in Fig. 1(a)]. Because of the very low carrier concentration, there are little additional deformations induced by the local interactions. The difference between the $G^0W^0$ and $GW$ + EDMFT treatment concerns mainly an increase in the local energy. The combination of these two effects yields a broadened Γ pocket, which has the highest intensity at $k_z = 0$ in the undoped compound [see Fig. 4(a)]. Moving to the intermediate value of $k_z = 0.25$ [see Fig. 4(b)], in addition to the dominant Ni-$3d_{x^2-y^2}$ contribution, we notice some spectral weight in the M-A direction (at the corners of the Brillouin zone), which has a Ni-$3d_{xz,yz}$ character. This feature is consistent with the charge susceptibility results for undoped $NdNiO_2$. Finally, at $k_z = 0.5$, we find significant deviations from the LDA result. The Ni-$3d_{x^2-y^2}$ pocket centered at the $Z$ point gives way to a Ni-$3d_{z^2}$ feature, as can be seen from the lobes

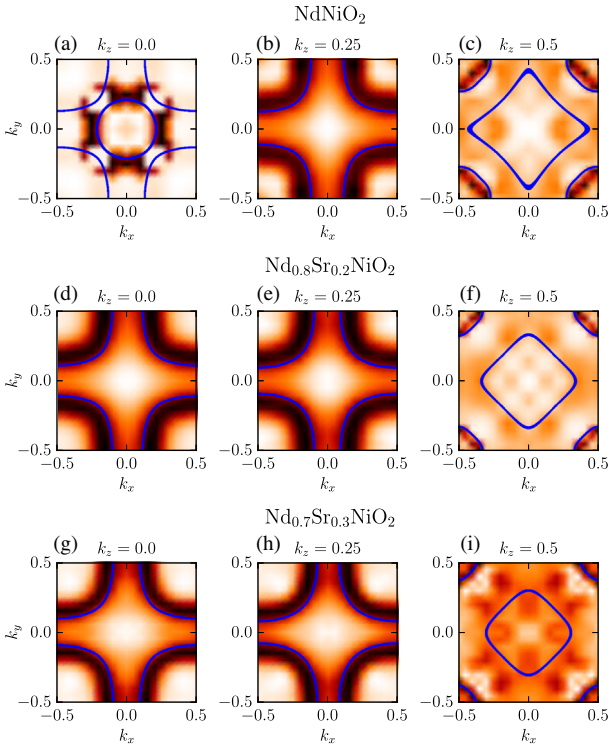


FIG. 4. Doping evolution of the Fermi surface. The blue lines show the LDA Fermi surfaces, while the intensity plots for the occupied states illustrate the "Fermi surfaces" of the interacting systems, calculated as the total spectral function at $\omega = 0$. Here, the intensity scale is relative to the maximum value of this function. Analogous orbital-resolved plots with a fixed intensity scale can be found in the SM [30].

emerging in the $Z$-$R$ direction. In this region, the dispersion is already flat at the LDA level, but, as several of our results suggest, the interaction effects significantly increase the local energy. Upon doping, the Γ pocket and the small M-A weight are removed, leaving the typical $d_{x^2-y^2}$ shape at $k_z = 0$, 0.25, while the lobes originating from Ni-$3d_{z^2}$ states persist. The latter indicates an active role of these states at the Fermi level in all the studied setups. A general observation is that the Fermi surface, and especially the Ni-$3d_{x^2-y^2}$ contribution, gets closer to the LDA result with increasing hole doping, which is consistent with the system becoming more metallic and less correlated.

### D. Optical and Hall conductivities

In Fig. 5, we present results for the optical and Hall conductivities computed for all the doping levels within linear response theory. In the limit of infinite dimensions [42], the irreducible vertex function becomes local, and it can be neglected when the current vertex is odd with respect to the **k** vector [43]. As a consequence, the Kubo formula for the conductivities requires the evaluation of bubblelike diagrams involving only the Green's functions and current vertices. The response function parallel to an

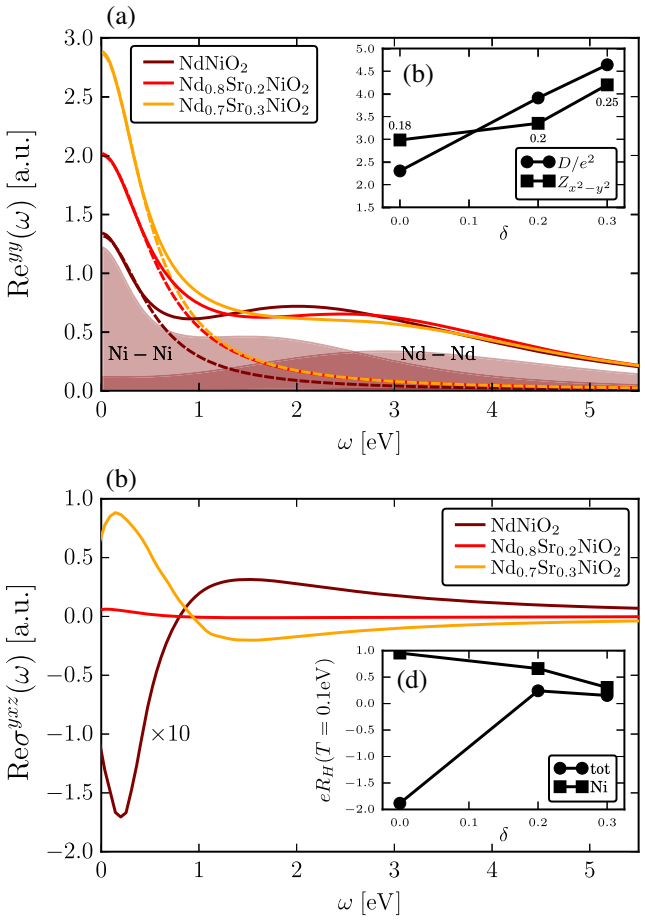


FIG. 5. Linear response conductivities. (a) Optical conductivity as a function of doping. The shading indicates the contribution of the two sites in the undoped compound. (b) Drude weight as a function of doping and comparison to the DMFT estimate of the mass enhancement for the Ni-$3d_{x^2-y^2}$ orbital (derivative of the local self-energy), with values indicated over the points. (c) Hall conductivity as a function of doping. The curve of the undoped system has been rescaled by a factor of 10 for better visibility. (d) Hall coefficient for the whole system and restricted to the Ni site only.

electric field in the $y$ direction is the optical conductivity $\mathrm{Re}\sigma^{yy}(\omega)$. In interacting systems, it features two contributions, a Drude-like peak at low frequency, originating from excitations within the quasiparticle band, and incoherent structures $\sigma^{\mathrm{inc}}(\omega)$ at higher energies stemming either from interband excitations or, for a correlated band, from excitations to the Hubbard satellites [44]:

$$\mathrm{Re}\sigma^{yy}(\omega) = \frac{D}{\pi}\frac{\tau}{1-(\omega\tau)^2} + \sigma^{\mathrm{inc}}(\omega), \tag{13}$$

where $\tau$ denotes the relaxation time and $D = e^2(n/m^*)$ is the Drude weight written in terms of the carrier density $n$ and effective mass $m^*$. Our results in Fig. 5(a) capture both the low- and high-energy peaks with weight that is transferred from the latter to the former as a function of hole doping. By separately computing the contributions from the Nd and Ni sites, we find that Nd yields a high-energy peak that is essentially fixed at $\omega \sim 3.5$ eV, regardless of the doping concentration, so the spectral weight transfer originates from Ni (see SM [30] for the site-resolved $\mathrm{Re}\sigma^{yy}$ at various doping levels). These observations demonstrate a more metallic behavior of the Ni subsystem with increasing hole doping, despite the almost constant occupation and the increase in the interaction parameters [Eq. (12)]. The weaker correlations result from the stronger increase in the interorbital interactions, compared to the intraorbital interactions, and the corresponding weakening of the Hund couplings; hence, they are a nontrivial manifestation of multiorbital effects. To quantify the degree of metallicity of the correlated multiorbital system, we extract the Drude weight and relaxation time by fitting the low-energy part of $\mathrm{Re}\sigma^{yy}(\omega)$ to Eq. (13). Note that $D$ is inversely proportional to an effective mass defined for the entire system and is shown in Fig. 5(b). The result indicates that doping indeed brings the system into a more-metallic, less-correlated state. This result is consistent with several measurements [2,3,17] that report a decrease in the resistivity with hole doping on the underdoped side of the $T_c$ dome, which appears to be least affected by disorder. In Fig. 5(b), we also plot the quasiparticle weight $Z_{x^2-y^2}$ obtained from the local self-energy of the Ni-$3d_{x^2-y^2}$ orbital. Both estimates are in qualitative agreement with the LDA + DMFT results reported by Kitatani *et al.* [14].

Our simulation results indicate that Hund-coupling-induced correlations are present at least up to $T = 0.1$ eV. This appreciable temperature is still lower than the relevant energy scales of the system, which, for the purpose of testing the multiorbital nature of the compound, are the energy separation between the $d_{x^2-y^2}$ local energy and the levels of the low-lying orbitals, as well as the Hund coupling. In the SM [30], we provide evidence that lowering the temperature further enhances the multiorbital features. While for the standard conductivity one needs to take the derivative of the free energy with respect to the vector potential twice, the Hall conductivity $\mathrm{Re}\sigma^{yxz}$ involves a third-order process, which requires an additional vertex insertion. In deriving the Hall current-current correlator, we extended (specifically for the $GW$ + EDMFT implementation) the approach described in Ref. [45] to the multiorbital case, as explained in the SM [30]. The Hall coefficient, defined as

$$R_H = \frac{\mathrm{Re}\sigma^{yxz}(0)}{\mathrm{Re}\sigma^{yy}(0)\mathrm{Re}\sigma^{xx}(0)}, \tag{14}$$

characterizes the nature of the charge carriers: It has a negative sign for electronlike Fermi surfaces, while it is positive for holelike ones. Our results for $R_H$, in units of the inverse electron density, are reported in Fig. 5(d) and are in

qualitative agreement with the recent experimental findings of Li *et al.* [2] and Zheng *et al.* [3].

## IV. CONCLUSIONS

To address the physics of doped $NdNiO_2$ in the normal state, and, in particular, the self-doping effect, we extended the recently developed $GW$ + EDMFT approach to multisite systems. This method has the significant advantage of being free from ill-defined double countings or arbitrary choices of interaction parameters. It captures the dynamical screening due to long-ranged and local charge fluctuations and self-consistently computes the local and nonlocal interactions appropriate for the low-energy model. Our results allow us to assert with confidence that undoped and hole-doped $NdNiO_2$ represent genuine multiorbital systems. Orbitals that, within a DFT description, are expected to be fully occupied and essentially inert are lifted closer to the Fermi level by the interactions. As a consequence, other orbitals than the naively expected Ni-$3d_{x^2-y^2}$ also become involved in low-energy charge fluctuations and in the formation of high-spin states. We find prominent contributions from $d^8$ and $|S_z| = 1$ local configurations, even in the undoped compound. The evolution of the metallicity with hole doping is a direct consequence of the doping-induced changes in the dynamically screened interorbital interactions. Therefore, a low-energy model consisting of a single $d$ orbital with fixed and static interactions misses important aspects of the physics of undoped and hole-doped $NdNiO_2$. On the other hand, the high-frequency (Hartree) limit of our approach seems to be consistent with the effective single-band picture, and in this sense, our results reconcile the two fronts of the debate. As a nontrivial check of our parameter-free *ab initio* formalism, we computed the optical and Hall conductivities within linear response theory and found qualitative agreement both with the reported decrease in the resistivity in the doping range least affected by disorder [2] and with the recently measured Hall coefficients [2,3].

At the temperature considered in this work ($T = 0.1$ eV), we found no trace of a magnetically ordered state. However, from our results, the presence of antiferromagnetic short-range correlations, or of long-range order at a lower energy scale, cannot be ruled out. In order to settle this issue, calculations at lower $T$ and a cluster extension of the $GW$-EDMFT approach would be desirable, but such simulations are currently prevented by technical limitations and are beyond the scope of the present study.

## ACKNOWLEDGMENTS

F. P., V. C., and P. W. acknowledge support from the Swiss National Science Foundation through NCCR MARVEL and the European Research Council through ERC Consolidator Grant No. 724103. F. N. and F. A. acknowledge financial support from the Swedish Research Council (Vetenskapsrådet). The calculations were performed on the Beo04/Beo05 cluster at the University of Fribourg. We thank F. Lechermann, A. J. Millis, and H. Y. Hwang for helpful discussions.

[1] D. Li, K. Lee, B. Y. Wang, M. Osada, S. Crossley, H. R. Lee, Y. Cui, Y. Hikita, and H. Y. Hwang, *Superconductivity in an Infinite-Layer Nickelate*, Nature (London) **572**, 624 (2019).

[2] D. Li, B. Y. Wang, K. Lee, S. P. Harvey, M. Osada, B. H. Goodge, L. F. Kourkoutis, and H. Y. Hwang, *Superconducting Dome in* $Nd_{1-x}Sr_xNiO_2$ *Infinite Layer Films*, Phys. Rev. Lett. **125**, 027001 (2020).

[3] S. Zeng, C. S. Tang, X. Yin, C. Li, Z. Huang, J. Hu, W. Liu, G. J. Omar, H. Jani, Z. S. Lim, K. Han, D. Wan, P. Yang, A. T. S. Wee, and A. Ariando, *Phase Diagram and Superconducting Dome of Infinite-Layer* $Nd_{1-x}Sr_xNiO_2$ *Thin Films*, Phys. Rev. Lett. **125**, 147003 (2020).

[4] V. I. Anisimov, D. Bukhvalov, and T. M. Rice, *Electronic Structure of Possible Nickelate Analogs to the Cuprates*, Phys. Rev. B **59**, 7901 (1999).

[5] K.-W. Lee and W. E. Pickett, *Infinite-Layer* $LaNiO_2$*:* $Ni^{1+}$ *Is Not* $Cu^{2+}$, Phys. Rev. B **70**, 165109 (2004).

[6] Y. Nomura, M. Hirayama, T. Tadano, Y. Yoshimoto, K. Nakamura, and R. Arita, *Formation of a Two-Dimensional Single-Component Correlated Electron System and Band Engineering in the Nickelate Superconductor* $NdNiO_2$, Phys. Rev. B **100**, 205138 (2019).

[7] E. Dagotto, *Correlated Electrons in High-Temperature Superconductors*, Rev. Mod. Phys. **66**, 763 (1994).

[8] M. Jiang, M. Berciu, and G. A. Sawatzky, *Critical Nature of the Ni Spin State in Doped* $NdNiO_2$, Phys. Rev. Lett. **124**, 207004 (2020).

[9] F. Lechermann, *Late Transition Metal Oxides with Infinite-Layer Structure: Nickelates versus Cuprates*, Phys. Rev. B **101**, 081110(R) (2020).

[10] J. Zaanen, G. A. Sawatzky, and J. W. Allen, *Band Gaps and Electronic Structure of Transition-Metal Compounds*, Phys. Rev. Lett. **55**, 418 (1985).

[11] W. Kohn and L. J. Sham, *Self-Consistent Equations Including Exchange and Correlation Effects*, Phys. Rev. **140**, A1133 (1965).

[12] H. Sakakibara, H. Usui, K. Suzuki, T. Kotani, H. Aoki, and K. Kuroki, *Model Construction and a Possibility of Cupratelike Pairing in a New* $d^9$ *Nickelate Superconductor* $(Nd, Sr)NiO_2$, Phys. Rev. Lett. **125**, 077003 (2020).

[13] F. Lechermann, *Multiorbital Processes Rule the* $Nd_{1-x}Sr_xNiO_2$ *Normal State*, Phys. Rev. X **10**, 041002 (2020).

[14] M. Kitatani, L. Si, O. Janson, R. Arita, Z. Zhong, and K. Held, *Nickelate Superconductors—A Renaissance of the One-Band Hubbard Model*, npj Quantum Mater. **5**, 59 (2020).

[15] P. Werner and S. Hoshino, *Nickelate Superconductors: Multiorbital Nature and Spin Freezing*, Phys. Rev. B **101**, 041104(R) (2020).

[16] A. Georges, G. Kotliar, W. Krauth, and M. J. Rozenberg, *Dynamical Mean-Field Theory of Strongly Correlated*

*Fermion Systems and the Limit of Infinite Dimensions*, Rev. Mod. Phys. **68**, 13 (1996).

[17] B. H. Goodge, D. Li, M. Osada, B. Y. Wang, K. Lee, G. A. Sawatzky, H. Y. Hwang, and L. F. Kourkoutis, *Doping Evolution of the Mott-Hubbard Landscape in Infinite-Layer Nickelates*, arXiv:2005.02847.

[18] F. C. Zhang and T. M. Rice, *Effective Hamiltonian for the Superconducting Cu Oxides*, Phys. Rev. B **37**, 3759 (1988).

[19] L. Boehnke, F. Nilsson, F. Aryasetiawan, and P. Werner, *When Strong Correlations Become Weak: Consistent Merging of GW and* EDMFT, Phys. Rev. B **94**, 201106 (R) (2016).

[20] F. Nilsson, L. Boehnke, P. Werner, and F. Aryasetiawan, *Multitier Self-Consistent GW + EDMFT*, Phys. Rev. Mater. **1**, 043803 (2017).

[21] F. Petocchi, F. Nilsson, F. Aryasetiawan, and P. Werner, *Screening from $e_g$ States and Antiferromagnetic Correlations in $d^{(1,2,3)}$ Perovskites: A GW + EDMFT Investigation*, Phys. Rev. Research **2**, 013191 (2020).

[22] P. Hohenberg and W. Kohn, *Inhomogeneous Electron Gas*, Phys. Rev. **136**, B864 (1964).

[23] L. Bellaiche and D. Vanderbilt, *Virtual Crystal Approximation Revisited: Application to Dielectric and Piezoelectric Properties of Perovskites*, Phys. Rev. B **61**, 7877 (2000).

[24] P. Sun and G. Kotliar, *Extended Dynamical Mean-Field Theory and GW Method*, Phys. Rev. B **66**, 085120 (2002).

[25] S. Biermann, F. Aryasetiawan, and A. Georges, *First-Principles Approach to the Electronic Structure of Strongly Correlated Systems: Combining the GW Approximation and Dynamical Mean-Field Theory*, Phys. Rev. Lett. **90**, 086402 (2003).

[26] L. Hedin, *New Method for Calculating the One-Particle Green's Function with Application to the Electron-Gas Problem*, Phys. Rev. **139**, A796 (1965).

[27] The FLEUR group, The FLEUR Project, http://www.flapw.de.

[28] M. A. Hayward and M. J. Rosseinsky, *Synthesis of the Infinite Layer* Ni(I) *Phase* $NdNiO_2 + x$ *by Low Temperature Reduction of* $NdNiO_3$ *with Sodium Hydride*, *Solid State Sci.* 5, 839 (2003).

[29] F. Aryasetiawan, M. Imada, A. Georges, G. Kotliar, S. Biermann, and A. I. Lichtenstein, *Frequency-Dependent Local Interactions and Low-Energy Effective Models from Electronic Structure Calculations*, Phys. Rev. B **70**, 195104 (2004).

[30] See Supplemental Material at http://link.aps.org/supplemental/10.1103/PhysRevX.10.041047 for orbital resolved occupations of the different setups.

[31] N. Marzari and D. Vanderbilt, *Maximally Localized Generalized Wannier Functions for Composite Energy Bands*, Phys. Rev. B **56**, 12847 (1997).

[32] A. A. Mostofi, J. R. Yates, Y.-S. Lee, I. Souza, D. Vanderbilt, and N. Marzari, *Wannier90: A Tool for Obtaining Maximally-Localised Wannier Functions*, Comput. Phys. Commun. **178**, 685 (2008).

[33] F. Freimuth, Y. Mokrousov, D. Wortmann, S. Heinze, and S. Blügel, *Maximally Localized Wannier Functions within the FLAPW Formalism*, Phys. Rev. B **78**, 035120 (2008).

[34] R. Sakuma, *Symmetry-Adapted Wannier Functions in the Maximal Localization Procedure*, Phys. Rev. B **87**, 235109 (2013).

[35] C. Friedrich, S. Blügel, and A. Schindlmayr, *Efficient Implementation of the GW Approximation within the All-Electron FLAPW Method*, Phys. Rev. B **81**, 125102 (2010).

[36] P. Werner, A. Comanac, L. de' Medici, M. Troyer, and A. J. Millis, *Continuous-Time Solver for Quantum Impurity Models*, Phys. Rev. Lett. **97**, 076405 (2006).

[37] H. Hafermann, P. Werner, and E. Gull, *Efficient Implementation of the Continuous-Time Hybridization Expansion Quantum Impurity Solver*, Comput. Phys. Commun. **184**, 1280 (2013).

[38] P. Werner and A. J. Millis, *Dynamical Screening in Correlated Electron Materials*, Phys. Rev. Lett. **104**, 146401 (2010).

[39] M.-Y. Choi, K.-W. Lee, and W. E. Pickett, *Role of* $4f$ *States in Infinite-Layer* $NdNiO_2$, Phys. Rev. B **101**, 020503(R) (2020).

[40] A. S. Botana and M. R. Norman, *Similarities and Differences between* $LaNiO_2$ *and* $CaCuO_2$ *and Implications for Superconductivity*, Phys. Rev. X **10**, 011024 (2020).

[41] M.-Y. Choi, W. E. Pickett, and K. W. Lee, *Quantum-Fluctuation-Frustrated Flat Band Instabilities in* $NdNiO_2$, Phys. Rev. Research **2**, 033445 (2020).

[42] T. Pruschke, D. L. Cox, and M. Jarrell, *Hubbard Model at Infinite Dimensions: Thermodynamic and Transport Properties*, Phys. Rev. B **47**, 3553 (1993).

[43] This is not, in general, valid for realistic dispersions, but, considering that the *GW* vertex function is a delta function and the EDMFT contribution is local, we consider this approximation to be accurate enough.

[44] M. Jarrell, J. K. Freericks, and T. Pruschke, *Optical Conductivity of the Infinite-Dimensional Hubbard Model*, Phys. Rev. B **51**, 11704 (1995).

[45] P. Voruganti, A. Golubentsev, and S. John, *Conductivity and Hall Effect in the Two-Dimensional Hubbard Model*, Phys. Rev. B **45**, 13945 (1992).